

To appear in the *Journal of Geophysical Research*, 1996.

Accuracy of the independent pixel approximation for satellite estimates of oceanic boundary layer cloud optical depth

L. H. Chambers and B. A. Wielicki

Atmospheric Sciences Division, NASA Langley Research Center, Hampton, Virginia

K. F. Evans

Program in Atmospheric and Oceanic Sciences, University of Colorado, Boulder

Abstract

A theoretical study has been conducted on the effects of cloud horizontal inhomogeneity on the retrieval of optical depth by remote sensing of visible reflectance. Forty-five Landsat scenes of oceanic boundary layer clouds provide a sampling of real cloud fields, including trade cumulus, open and closed cell broken stratocumulus, and solid stratocumulus. The spherical harmonic discrete ordinate method (SHDOM) radiative transfer model is used to calculate two-dimensional reflectances from subsampled cloud strips representing the Landsat scenes. The independent pixel approximation (IPA) is used to retrieve optical depth for comparison to the original input. Results for τ_{IPA} versus τ_{ref} are presented on scales from the Landsat pixel scale (28.5 m) to an imager pixel scale (6 km) to near mesoscale (60 km). The random error decreases as the averaging scale increases, but error due to inhomogeneity remains. At the 60 km scale the average error is about 6% for high Sun, 2% for low Sun. Individual scenes, however, have retrieved optical depth errors as high as 45% due to horizontal radiative transport. The ability to retrieve higher statistical moments of the frequency distribution of optical depth is also assessed. Sigma, (σ), the standard deviation of τ , is retrieved quite well up to a point, then is underestimated due to the smoothing effect of horizontal radiative transport. The gamma function parameter ν , another measure of the width of the τ frequency distribution, is retrieved quite well over a wide range but with a systematic bias which varies with solar zenith angle, again due to horizontal radiative transport. A method is sought to reduce the optical depth retrieval error using a simple correction based on remotely sensed cloud properties. Of those considered, cloud physical aspect ratio (computed here from one possible relation which depends on properties obtainable from remote sensing) is found to be the most effective correction parameter. The aspect ratio correction reduces the retrieved optical depth bias error by 50 to 100% and the RMS error by 20 to 50%. Correction coefficients are presented at three solar zenith angles. This work is limited by its consideration of only single-level marine boundary layer clouds, assumptions of conservative scattering, constant cloud droplet size, no gas absorption or surface reflectance, and restriction to two-dimensional radiative transport. Future work will attempt to remove some of these limitations. The Landsat data used are also limited due to radiative smoothing.

1. Introduction

One of the key uncertainties in climate modeling is the role of clouds in the Earth's radiation balance. Results from the Earth Radiation Budget Experiment (ERBE) have shown that clouds can cause either a warming or a cooling of the atmosphere, depending on their location and properties. Global monitoring of clouds from satellites is therefore essential to accurate climate prediction. Before we can use satellite cloud property data to test cloud models, however, we need an assessment of the accuracy of the satellite-derived cloud properties. The present paper investigates the impact of using plane-parallel theory to convert measured satellite visible reflectances into estimates of cloud optical depth at visible conservative scattering wavelengths. *Pincus et al.* [1995] provides a complementary study, evaluating other contributors to the remote sensing error.

Cloud fields provide an endless variety of optical properties, not only in terms of vertical variation but also horizontal variations. Simple non-plane-parallel cloud shapes and regular fields of simple clouds have been studied in depth using analytical and computational methods [e.g., *McKee and Cox*, 1974; *Davies*, 1978; *Welch and Wielicki*, 1984; *Gabriel et al.*, 1993; *Kobayashi*, 1993; *Killen and Ellingson*, 1994; *Takara and Ellingson*, 1996].

Recently, studies have begun to use more realistic horizontal variations of cloud optical properties derived from passive microwave observations [*Cahalan et al.*, 1994b], radar and lidar observations [*Stackhouse*, 1995], and large eddy simulation dynamical cloud models [*Duda and Stephens*, 1994]. Other studies [*Nakajima et al.*, 1991] have compared remotely sensed optical depth data to that inferred from in situ aircraft measurements and found the largest uncertainties in converting in situ data to optical depth. Yet another approach [e.g., *Davis et al.*, 1996; *Marshak et al.*, 1995b] is to use statistically based models of overcast cloud variability to study horizontal transport effects. *Cahalan et al.* [1994b] showed that the independent pixel approximation (IPA) provides a reasonable estimate of the mesoscale-average properties of marine boundary layer clouds, at least for overcast conditions near the coast of California. The IPA simply assumes that each observation (satellite field of view, or surface instrument observation point) can be treated as if it were, in fact, a horizontally homogeneous cloud, thereby ignoring the horizontal photon transport between fields of view but capturing

the nonlinear relationship between cloud optical depth and cloud albedo which can itself be a large source of error in global climate models. The work of *Duda and Stephens* [1994] and *Stackhouse* [1995] tested the IPA assumption using two-dimensional radiative model calculations [*Evans*, 1993] for two cirrus cloud and oceanic boundary layer cloud cases and found significant pixel level errors in cloud optical depth, but small domain average errors, similar to the results of *Cahalan et al.* [1994b].

To date such work has been limited to studies of a few cloud cells, or to the simpler case of overcast clouds. The objective of the present study is to extend the earlier results to a much wider range of marine boundary layer cloud conditions, including broken stratus and trade cumulus cases, found in 45 Landsat scenes of clouds over various oceanic regions. (Note that each scene contains the same amount of data as a land-based instrument operating at 10 Hz 24 hours per day for almost 5 days.) In turn, 20 samples are taken from each Landsat scene, so that a total of 900 cloud realizations are considered. Computations of the radiance field using both IPA and two-dimensional radiative models are performed. The calculations are used to assess the internal consistency of the IPA assumption for realistic cloud fields.

A limitation of the current work is that the IPA is used initially to derive the Landsat optical depth distributions which are used as the reference field for computing two-dimensional radiance fields. In this case, the test is a necessary but not sufficient condition for verification of the IPA assumption. Furthermore, since only two-dimensional cloud fields are considered here (effectively, cloud streets), the full three-dimensional effect of realistic cloud fields has not been captured, neither have the effects of multiple cloud layers been included. The present results can be thought of as a minimum error bound for the effect of cloud inhomogeneity on satellite-derived cloud optical depth for marine boundary layer clouds.

Finally, what is the impact of the errors in satellite-derived optical depth on the testing of global climate models? The work of *Cahalan et al.* [1994b] demonstrates clearly the need for the measurement and prediction of not only the grid box average of the cloud optical depth but also higher moment statistics to specify the probability distribution of optical depth, even for cloud fields accurately represented by the IPA. While *Cahalan et al.* [1994b] found overcast stratocumulus clouds to be well represented by lognormal probability density functions, *Wielicki and*

Parker [1994] found that nonovercast cases of marine boundary layer cloud showed no modal cloud optical depth and were not well represented by lognormal distributions. Recently, *Barker et al.* [1996] have shown that gamma functions can represent the range of distributions found in the *Wielicki and Parker* [1994] results and have suggested a gamma-IPA model, which allows calculation of grid box average radiative fluxes with little additional computational expense over traditional plane-parallel two-stream calculations. These results suggest the following hierarchical levels of accuracy in radiative transfer modeling of realistic cloud fields:

plane parallel \Rightarrow gamma IPA \Rightarrow IPA \Rightarrow 2D \Rightarrow 3D

where in the next few years we may see global models shifting from plane-parallel calculations to those which assume some functional form for the probability density function of cloud optical depth, either the gamma function suggested by *Barker* or some other functional form. Cloud formation models, of course, will be required to predict a higher-order “closure” for the variability of sub-grid-scale cloud properties. The results of *Wielicki and Parker* [1994] suggest that the form of the probability density function appropriate for a general circulation model (GCM) grid box may, in fact, be a systematic function of grid box cloud fraction. In order to assess the ability to remotely sense these higher-order statistical moments, this paper will derive remote sensing errors for both the average optical depth and the standard deviation of optical depth, and for the gamma function fit suggested by *Barker et al.* [1996].

Section 2 describes the two-dimensional cloud fields inferred from Landsat. Section 3 describes the numerical radiation model as well as the radiative quantities studied in this work. Section 4 discusses the errors in IPA-derived cloud optical depth and distribution as a function of spatial scale. Section 5 begins to address the question of correcting the optical depth retrieval errors. Section 6 summarizes the major conclusions.

2. Landsat Inferred Horizontal Inhomogeneity

2.1. Scene Selection

Selection of the Landsat data to analyze was performed by examining several hundred Landsat images on microfiche or hardcopy prints, to select a wide range of cloud fraction, cell size, cell horizontal as-

pect ratio, as well as closed and open cellular convection cases. In this sense, the intent of the data set is not to represent the climatology of any particular region of the Earth but rather to reasonably cover the range of oceanic boundary layer cloud variability which might be observed from space. After acquisition of the digital data for each Landsat scene, the Landsat band 6 thermal infrared data for clear and optically thick portions of the cloud fields was used to confirm that the difference between clear sky temperature and cloud temperature was typical of those expected for boundary layer cloud fields. Cases not included in this data set are boundary layer clouds over land, snow or ice, or any boundary layer cloud cases which showed evidence of middle- or high-level clouds. The primary test for the existence of multi-layer cloud was the examination of frequency distributions of $0.83 \mu\text{m}$ reflectance versus $11 \mu\text{m}$ brightness temperature. Multiple branches of these distributions would indicate the presence of multiple cloud layers with varying emission temperatures. Not unexpectedly, the majority of the cases found were subtropical oceanic boundary layer cloud.

Finally, it was desired that the cloud fields be reasonably statistically homogeneous over the analyzed region. In other words, areas with large qualitative changes in cloud cell size, orientation, or cloud cover were avoided. The practical result of this last requirement was that the 180 km Landsat scene was typically too large to meet the qualitative statistical homogeneity criteria. Therefore a smaller analysis area was chosen (58.4 km or 2048 by 2048 pixels). This smaller analysis region allowed a marked improvement in the statistical homogeneity of the cloud fields. While this observation is purely subjective at present, it suggests that ultimately, successful modeling of boundary layer clouds as statistical ensembles may require global atmospheric models with grid box sizes measured in tens of kilometers (i.e., mesoscale) rather than the current 100s of kilometers. For the present study of the effects of non-plane-parallel radiative transfer, statistical homogeneity of the analysis data should enhance the statistical stability of the results and decrease the number of sample cases needed to represent a given cloud field.

As a result of this selection process, 52 Landsat scenes of marine boundary layer clouds were available for this study. The scenes were chosen to represent a wide range of boundary layer cloud types, including trade cumulus, open and closed cell broken stratocumulus and solid stratocumulus. A few representative

scenes of each type are reproduced in Plate 1. Dominant cell sizes range from less than 1 km to 30 km. Again, these cases do not represent the frequency of occurrence for any particular location. Identification of scenes 1–45 appeared in the work of *Harshvardhan et al.* [1994]. The additional scenes studied in this paper are summarized in Table 1. Of the scenes presented by *Harshvardhan et al.* [1994], seven were rejected because over 10% of the pixels were saturated in reflectance. These are scenes 1, 13, 20, 25, 26, 27, and 42. For the remaining scenes the mean saturation is 1.1%, with a minimum of zero saturation and a maximum of almost 7%.

2.2. Generating Cloud Properties

The Landsat data are converted from digital counts to spectral radiance and, finally, to an equivalent Lambertian reflectance as described by *Wielicki and Parker* [1992]. The clear sky reflectance and cloud threshold are then determined and are used to separate the Landsat image into clear and cloudy pixels as for the reference cloud cover determination in *Wielicki and Parker* [1992]. For each cloudy flagged pixel the Landsat nadir reflectance at 0.83 μm wavelength is converted to an estimate of cloud optical depth (τ). This is step 1 in Figure 1. The methodology for determination of optical depth is described by *Harshvardhan et al.* [1994] and assumes that each Landsat cloudy pixel can be assumed to be a plane-parallel cloud (IPA assumption). Conversion of reflectance to optical depth is based on interpolation in a lookup table derived using the DISORT multiple-scattering model [*Tsay et al.*, 1990] for monochromatic radiation at 0.83 μm . Retrieved optical depths can vary from 0.082 to 100 depending on the cloud detection limit and the maximum reflectance in the cloud field. Because of the relative insensitivity of reflectance to optical depth for values above 100, optical depths are limited to a maximum retrieved value of 100. A very small portion (less than 0.1%) of the Landsat data in this study exceeded this limit. The maximum optical depth saturation for any given scene is less than 2%; for most scenes it is zero.

While the above procedure provides an estimate of the horizontal variability of cloud optical depth, derivation of a two-dimensional (vertical, horizontal) distribution of cloud extinction coefficient (step 2 of Figure 1) is required for the two-dimensional radiative computations. This is achieved by using an empirical relation from *Minnis et al.* [1992] to convert optical depth for each Landsat pixel into an estimate of the

physical thickness Δz of the cloud in kilometers

$$\Delta z = 0.08\sqrt{\tau} - 0.04 \quad (1)$$

The minimum cloud thickness is set to 20 m, consistent with Clouds and the Earth’s Radiant Energy System (CERES) plans [*Baum et al.*, 1995]. This relation is discussed further in section 2.3.1.

An extinction coefficient β can then be calculated for each pixel and distributed through the cloud depth. For this study, the cloud is assumed to have uniform extinction with height in each pixel; that is, $\beta = \tau/\Delta z$. This extinction field must then be discretized onto the computational grid points while maintaining the integrated column optical depth at the Landsat value assuming linear interpolation between grid points. If the vertical grid spacing is dz_g , then an unbiased discretized extinction coefficient is given by

$$\beta_g = \frac{\tau}{(N_g - 1/2)dz_g} \quad (2)$$

where N_g , the number of grid points within the cloud, is at least 30 so that the discretization does not change the value of β more than a few percent. This choice also ensures sufficient grid resolution in the thinnest (20 m) clouds. The cloud top height is held constant, while the cloud base varies according to the calculated Δz . For inversion-capped boundary layer clouds over ocean, this is considered more physically realistic than a constant base height assumption.

Conservative scattering ($\omega_0 = 1$) has been assumed throughout this study (at the 0.83 μm wavelength used in the computations for this paper the actual single-scattering albedo is 0.99997). A Mie phase function for a gamma distribution of water droplets with an effective radius r_e of 10 μm and an effective variance of 0.1 is used, consistent with the International Satellite Cloud Climatology Project (ISCCP) [*Rossow et al.*, 1991]. The cloud particle size distribution is assumed not to vary throughout the cloud. While unrealistic (measurements by *Nakajima et al.* [1991], for example, show that the form of $r_e(z)$ can vary widely), the treatment of vertical variability in the cloud has been deferred to a later study. The effect of atmospheric gases on the radiation within the cloud is also neglected.

From each Landsat scene, a series of 20 randomly placed horizontal scan line samples is taken (see Figure 2). Each scan line sample is 200 pixels (5.7 km) long. Representative scan line sample cloud profiles for overcast and broken cloud fields are shown in Figure 3. This sampling is required because computing

the entire scene is currently beyond the bounds of computer resources in terms of both time and memory. The parameter $\sum \bar{\tau}_{\text{IPA}} / \sum \bar{\tau}_{\text{ref}}$, using cloud fraction (A_c) weighted averaging for ns scans, where

$$\sum \bar{\tau}_{\text{ref}}(ns) = \frac{\sum_{n=1}^{ns} \bar{\tau}_{\text{ref}} * A_{c_n}}{\sum_{n=1}^{ns} A_{c_n}} \quad (3)$$

and the scan line sample mean is for cloudy pixels only; that is,

$$\bar{\tau}_{n_{\text{ref}}} = \frac{\sum_p \Phi_p \tau_{p n_{\text{ref}}}}{\sum_p \Phi_p} \quad (4)$$

where $\Phi_p = 0$ for $\tau = 0$, and $\Phi_p = 1$ for $\tau > 0$, with similar expressions for the independent pixel sum, is used to assure that the subsampling is representative of the entire scene. A convergence history versus number of scan line samples ns is shown in Figure 4 for a representative Landsat scene. (Missing symbols in this figure indicate scan line samples that were found to be completely cloud free.) In most of the scenes, convergence is reached with five to ten scan line samples, though some of the more varied scenes require 15 scan line samples for this parameter to converge. In all cases, however, all 20 scan line samples are included.

Note that while in some cases sampling the scenes with vertical scan line samples, or scan line samples in a random orientation, might have produced some differences in cloud fields, for the purposes of this work, horizontal sampling is considered to be sufficient to generate a set of representative two-dimensional fields.

Since a cyclical boundary condition is imposed in the two-dimensional solution, three logarithmic interpolating points are added on the right-hand side of most scan line samples to blend the cloud field from scan edge to scan edge. In some cases (about 6% of the samples) this still results in an edge gradient of optical depth which exceeds the maximum gradient found in the interior of the 20 scan line samples for that scene. This is considered unrealistic; therefore additional interpolating points (1 to 10 additional points) are added in these few cases until the edge gradient is no greater than the largest interior gradient.

2.3. Sensitivity Studies

Four representative scenes have been used to investigate the sensitivity of the results to a number of issues. Scene 28 represents the scattered cloud scenes,

scene 43 the broken cloud cases, and scene 39 overcast conditions. In addition, scene 32 was included in these studies because it is the most extreme cloud field in this data set.

In general, there is some solar zenith angle at which the optical depth retrieval error is essentially zero. This is the angle for a particular set of clouds at which leakage from the cloud sides balances solar energy entering cloud sides. To avoid ambiguity from this effect, a range of solar zenith angles should be included in studies of remote sensing retrieval error. Sensitivity to the following variables is assessed using the solar zenith angle with the greatest sensitivity to each particular change.

2.3.1. Cloud Thickness. The four test scenes were run assuming a cloud thickness fixed at about the maximum cloud thickness predicted by equation (1) for each scene: 200 m for scenes 28 and 43, 300 m for scene 39, and 750 m for scene 32. The results at $\theta_0 = 63^\circ$ are most sensitive, with optical depth retrieval error almost doubling for scattered cloud scenes and increasing 350% for scene 32. This finding makes sense, as the assumption of a constant cloud thickness overemphasizes the effect of cloud sides, particularly for low Sun.

In contrast, equation (1) is based on simultaneous satellite and ground-based data averaged to a 30 km scale. Its application to a 30 m Landsat pixel is not ideal but does provide the expected behavior of Δz : cloud physical thickness generally increases with cloud optical thickness. As a test of the relation, equation (1) has been applied to each pixel in the Landsat scenes, then averaged over the scene. This thickness is then compared to the result of equation (1) using a scene average optical depth, i.e., on the scale for which it was developed. The results show that the pixel scale application of equation (1) may underestimate the cloud thickness of the order of 10%. This bias is felt to be much preferable to the hundreds of percent biases which occur with the assumption of constant cloud thickness in nonovercast scenes.

2.3.2. Scan Length. The addition of interpolating points on the end of a scan line sample and the use of the periodic boundary condition have the potential to bias the results. To check this, the four test cases were run with scan line samples twice as long (400 pixels or 11.4 km). The results change by only a few percent, except for scene 32 where for low Sun the optical depth retrieval error almost triples. In that extreme scene the sampling of cloud edges is the overwhelming factor. This suggests that in future

studies with more vertically developed clouds, longer samples will be required.

2.3.3. Radiative Smoothing. *Marshak et al.* [1995a] have recently shown an apparent scale break in Landsat data around 200 m and suggest that radiative smoothing at that scale reduces the variability of any property retrieved on a smaller scale. To test whether this is a factor in the results presented here, the Landsat radiances were degraded to 228 m resolution. The degraded radiances were then used, as before, to generate a reference optical depth field. A bounded cascade model [*Cahalan et al.*, 1994a] with the appropriate parameters ($f = 0.3, 0.6, 0.8$ for overcast, broken, and scattered fields, respectively, and spectral slope = 1.66) was used to generate a two-dimensional (x and y) fractal field. For each sampled optical depth in the degraded scan line sample (now 25 “pixels” long), a string of eight fractal values was randomly chosen from the fractal field, normalized, then used to modulate the degraded optical depth. This provides a scan line sample with the gross features of the Landsat scene but with more variability below the characteristic smoothing scale. Results on the scan line sample scale change only a few percent, except for scene 32 where at high Sun there is almost a factor of 2 reduction in retrieval error. For this scene and to some extent for scene 28 representing the scattered cloud fields, a more sophisticated application of the cascade model to broken cloud fields would yield closer agreement. However, even this simplistic application shows that variability in the Landsat scenes below the radiative smoothing scale does not lead to significant underprediction of the optical depth retrieval error as presented in this paper on a scan line sample (5.7 km average) or larger scale.

Wave number spectra of several Landsat scenes have also been compared to those found in the work of *Davis et al.* [1996]. The Landsat data exhibit a range of slopes in their energy spectra, not inconsistent with the *Davis et al.* [1996] findings for overcast cases. For broken cloud cases, however, there tends to be a much smaller, if any, range of scale invariance (i.e., constant spectral slope). This feature does not appear to be related to any radiative smoothing of the Landsat data.

3. Radiative Model

3.1. Spherical Harmonic Discrete Ordinate Method

SHDOM, the spherical harmonic discrete ordinate method combines the aspects of the spherical harmonic and discrete ordinate representations of the radiation field that are most appropriate for radiative transfer. As with the spherical harmonic spatial grid (SHSG) method [*Evans*, 1993], the radiance field is represented on a discrete grid and the spherical harmonic representation is used to compute the scattering integral quickly. SHDOM, however, solves the integral form of the radiative transfer equation, computing radiance from the source function along discrete ordinates throughout the grid. While the spherical harmonic representation is faster and more accurate for the angularly smoothing operation of scattering, discrete ordinates are the best representation for the physical streaming of radiation. Details of the method are presented in the appendix.

3.2. Application

The two-dimensional (x and z) cloud fields generated from the Landsat scenes are provided as input to the SHDOM code. A solution (step 3 of Figure 1) is obtained with $L = 11$ zenith terms, and $M = 11$ azimuthal terms for the spherical harmonic truncation, and with $N_\mu = 12$ zenith angles and $N_\phi = 24$ azimuth angles in the discrete ordinate discretization. Using the TMS method of *Nakajima and Tanaka* [1988] and the delta-M method [*Wiscombe*, 1977] for the phase function, this truncation has been found to provide good accuracy (within 2% RMS) for the radiances. A Monte Carlo method has been used to verify the results for two typical broken cloud scan line samples, showing agreement within the uncertainty of the Monte Carlo solution using 20 million photons. Along with prior work by one author (*Evans*), this is considered sufficient verification of the SHDOM numerical model.

For each scan line sample of each scene, solutions are obtained for solar zenith angles, θ_0 , of 0° , 49° , and 63° ($\mu_0 = 1, 0.65, 0.45$), and with both the IPA and the two-dimensional solution options. Results used in this study are the nadir radiances as a function of x , representative of the Landsat radiance data. Sample radiance versus x profiles for overcast, broken cloud, and high aspect ratio scenes are shown in Figure 5 to illustrate the pixel by pixel differences between the IPA and two-dimensional solutions and the range of

cloud variability in this study.

3.3. Nadir Reflectance

The nadir reflectance $R(\mu = 1, \theta_0)$ is given by

$$R(\mu = 1, \theta_0) = \frac{\pi I(\mu = 1, \theta_0)}{\mu_0 F_\odot} \quad (5)$$

where I is the radiance and F_\odot is the incident solar flux. In the absence of two- or three-dimensional effects, R is a monotonically increasing function of τ , as shown in Figure 6. This function can be used to retrieve $\tau_{\text{IPA}}(x)$ from the computed $R_{2\text{D}}(x, \mu = 1, \theta_0)$ at each point along the scan line sample (step 4 of Figure 1). Here $R_{2\text{D}}$ approximates the satellite measured reflectance from each pixel within a cloud scene. The retrieved τ_{IPA} is based on the assumption of negligible horizontal photon transport (IPA assumption). Differences between τ_{IPA} and τ_{ref} used in the two-dimensional calculations indicate a violation of the IPA assumption and are used in section 4 to evaluate the errors in this assumption.

3.4. Aspect Ratio

It became clear early in this study that mean cloud optical depth and cloud fraction alone were not enough to describe the variety of cloud fields in the Landsat data. A method was therefore sought to estimate the aspect ratio of the cloud fields in a manner that could be remotely sensed from space. Aspect ratio was chosen as an additional parameter because of the impact that the local geometry of the clouds has on the character of the radiative transfer. For example, tall narrow clouds behave differently radiatively than short wide clouds.

Testing with simple periodic waves led to a method providing linear dependence on the amplitude and wavelength of the input field. For half-sine waves (negative portion set to zero) it measures exactly the wave height divided by the width at halfmaximum. For sine-squared, sine-cubed, or triangular waves the horizontal distance given by the denominator is at a point somewhat above or below the halfmaximum, between one third and two thirds of the wave height. The expression used is

$$\overline{\left(\frac{v}{h}\right)} = \frac{\Delta z_{\text{max}}}{2\Delta x(\rho(\Delta z) = 1/e)} \quad (6)$$

This is the ratio of the maximum amplitude divided by twice the distance at which the autocorrelation coefficient ρ of Δz falls to $1/e$. The value $1/e$ has been

shown to define an effective independence distance in a red-noise time series [Leith, 1973]. Several studies have demonstrated red spectra for both cloud liquid water path and Landsat cloud reflectances [Cahalan and Snider, 1989; Davis et al., 1996; L. Parker and B. A. Wielicki, personal communication, 1996].

Other possibilities tried were edge detection schemes, which suffer the problem of having no clear way to develop a scan line average; optical property-based schemes, which provide no information on cloud cell size; and schemes based on mean dimensions, which also provide no information on cell size. While equation (6) is not perfect, it is the most useful of the choices so far considered. Further study in this area might be fruitful.

An average aspect ratio is computed for each scan line sample from equation (6). This definition measures the ratio of the largest vertical cloud extent to a horizontal width which approximates the largest feature width at halfmaximum for the sample. An example is shown in Figure 7. Scan line samples which are completely clear over the 5.7 km sample have an aspect ratio of zero. The aspect ratio for completely overcast scan line samples is computed from the largest vertical cloud extent divided by the full 5.7 km sample width.

4. Consistency of IPA-Derived and Reference Optical Depths

For each scan line sample of each scene, following the first four steps in Figure 1, τ_{IPA} is retrieved as a function of x from the R - τ curve in Figure 6 for comparison to τ_{ref} . If $R_{2\text{D}}$ exceeds the maximum reflectance at that Sun angle, the optical depth is arbitrarily set to 100.

4.1. Instantaneous Pixel Level Errors

At the pixel level (28.5 m scale), the difference between the retrieved τ_{IPA} and the input τ_{ref} can be quite substantial. This behavior is pertinent to cloud property retrieval from, for example, the MODIS instrument. Scatterplots at $\theta_0 = 0^\circ$ and 63° are given in Plates 2a and 2b, respectively. While a large number of points fall near the diagonal, a substantial portion are far from it. These come from cases where horizontal radiative transport is important. Above the diagonal the clouds tend to be relatively large closely spaced cells, where multiple interactions between cloud sides lead to the reflection of more solar energy. Below the diagonal are small cloud cells where

loss of energy out cloud sides becomes important and results in lower reflection. Also shown in these figures are least squares fits to the scattered data points in the three cloud classes described below, suggesting that leakage out cloud sides dominates this cloud sample. Note that *Nakajima et al.* [1991] found a similar effect by adding gas absorption in a plane-parallel model. The average error in retrieved τ is about 20%. This is of the order of the error found in the work of *Pincus et al.* [1995] due to digitization and instrument calibration uncertainties (but note that both these errors will be reduced in the CERES time frame). The maximum error due to horizontal inhomogeneity is several times larger, confirming the Pincus statement that this is the largest uncertainty in cloud property retrieval.

The statistics of the differences are summarized in Table 2. The scenes are placed in three nearly equal-sized groups based on cloud fraction. For scenes with cloud fraction below 40% the variability of the difference between τ_{IPA} and τ_{ref} is of the same order as the mean cloud optical depth itself. For higher cloud fractions it falls to half the $\langle \bar{\tau}_c \rangle$ value; and for overcast clouds, it is only about 10%. Dependence on solar zenith angle is small. The large pixel-to-pixel variability in τ_{IPA} versus τ_{ref} is due to the local horizontal transport of radiation. Spatial averaging, even over a small scale, reduces the difference dramatically, as shown in Figure 8a. Here IPA and reference optical depths averaged according to equation (4) over a scan line sample (5.7 km) are compared for $\theta_0 = 0^\circ$. There are no points above the diagonal in this figure, indicating that for the cloud fields under study, interactions between adjacent cloud sides are swamped by loss of energy out the cloud sides. At $\theta_0 = 63^\circ$, Figure 8b, points do appear above the diagonal, because at this lower Sun angle, the cloud sides intercept and return some incoming solar radiance, and this effect dominates energy loss from cloud sides in at least some scan line samples.

4.2. Mesoscale Level Errors

Scene average results provide an idea of the error incurred, on the average, by a satellite as it overflies a regional area. They also provide some indication of errors on a scale close to that of a GCM grid box. The 20 samples for each scene have been averaged therefore according to equation (3) to provide 45 regional or mesoscale results.

4.2.1. Optical depth error. The scene average retrieved optical depth is plotted against the reference

scene optical depth in Figure 9. For most scenes the results are very close. In scenes with significantly different retrieved optical depth the variation decreases systematically with Sun angle, due to incoming sunlight intersecting cloud sides as well as the cloud top. Sunlit sides of clouds tend to overestimate τ_{ref} , while shadowed cloud sides show the opposite behavior. No such compensation exists for the overhead Sun case.

The statistics of the optical depth differences on this scale are given in Table 3, again in the three cloud cover classes. The standard deviation of the difference, $\sigma(\tau_{\text{IPA}} - \tau_{\text{ref}})$, drops a factor of 3 to 5 from that at the pixel level, reflecting the effect of averaging out local horizontal radiative transport. The mean difference in optical depth itself, $(\tau_{\text{IPA}} - \tau_{\text{ref}})$, is always negative. This indicates a bias in the IPA model. This bias and $\sigma(\tau_{\text{IPA}} - \tau_{\text{ref}})$ decrease with either increasing cloud cover or increasing solar zenith angle, as should be expected. Either parameter as it increases produces a smoother-looking cloud field in which horizontal radiative transport is less important.

Averaging all 45 scenes together, the ratio of optical depths $\bar{\tau}_{\text{IPA}}/\bar{\tau}_{\text{ref}}$ is 0.948, 0.942, and 0.979 for $\theta_0 = 0^\circ$, 49° , and 63° , respectively. Thus the overall error in retrieved optical depth in this sampling of cloud fields is 6% or less. There are scenes, however, with errors up to 25%; and the largest error is near 45% on a scene average basis for overhead Sun (see Figure 9). Again, these errors are of the order of the largest errors found by *Pincus et al.* [1995]. The scenes with the larger errors are generally winter time cases where the cloud top is above 2 km. Optical depth is large in these strongly thermally forced boundary layer clouds.

4.2.2. Statistical moment error. In addition to $\bar{\tau}$, it is important to determine the accuracy with which higher statistical moments can be retrieved for the scene average frequency distribution of τ . Results are given in Figures 10 and 11 for two relevant parameters: the standard deviation of cloud optical depth σ and the gamma function parameter $\nu = (\bar{\tau}/\sigma)^2$ [Barker et al., 1996], which is a measure of the width of the optical depth distribution. The standard deviation σ is well retrieved up to about 15. Beyond this point, the IPA retrieval substantially underestimates the variability of the cloud scene. This behavior should be expected, based on the sample reflectance profiles shown in Figure 5, which illustrate the smoothing effect of horizontal radiative transport.

The retrieved values of ν in Figure 11 compare quite well with ν_{ref} over a very large range of values

but with a systematic overestimate by the IPA which averages 24% at $\theta_0 = 0^\circ$ and 16% at $\theta_0 = 49^\circ$. At $\theta_0 = 63^\circ$, the mean difference is around 5%, but ν is distributed above and below the reference value. This is consistent with a general smoothing of the field by the two-dimensional solution. The worst agreement occurs for $\nu < 1$, where the variability of the scene is large relative to the mean optical depth. Statistics of the ν difference are shown in Table 3.

Ensemble probability distributions of optical depth at $\theta_0 = 0^\circ$ for small (0.-0.4), moderate (0.4-0.99), and high (0.99-1.) cloud fraction scenes are given in Figures 12a through 12c, respectively. These categories correlate roughly with trade cumulus, broken stratocumulus, and solid stratocumulus cloud types. Also shown in these figures are the mean (vertical bars) and standard deviation (horizontal bars) of the distributions. In all three cloud classes the standard deviation of the IPA is smaller, consistent with smoothing of the field by horizontal radiative transport, and the overcast result in Figure 12c compares well with a similar result in the work of *Marshak et al.* [1995b]. It should be remembered that the reference distribution in these figures already includes some effect of radiative smoothing of the Landsat-measured reflectance. The true distribution of optical depth should be somewhat broader. Note (Table 3) that these three cloud types occur in quite distinct ranges of ν . A value greater than 1 implies the existence of a mode in the gamma distribution and is consistent with overcast cloud fields. For 0-40% cloud cover the value of ν indicates no mode in optical depth, while for 40-99% cloud cover, the distribution should be approaching a modal one.

5. Correcting Optical Depth Retrieval

The question arises whether, given some knowledge of the effects of horizontal radiative transfer, it is possible to find a simple scheme to reduce the error in the retrieved optical depth. The present results are now examined in search of such a scheme.

A contour plot of the distribution of scan line samples in the aspect ratio-logarithm of optical depth space is shown in Figure 13. Note that the realistic cloud fields generated from the Landsat data do not uniformly fill the parameter space of this study. For example, very thin clouds do not occur with a large aspect ratio.

Results for the ratio $\overline{\tau_{\text{IPA}}}/\overline{\tau_{\text{ref}}}$ averaged over a scan line sample then sorted in terms of these two cloud

parameters are shown in Figure 14a at $\theta_0 = 0^\circ$. At this solar zenith angle the trends are quite clear. The ratio departs from one, indicating the effect of horizontal inhomogeneity, as τ increases and as aspect ratio increases. It varies from a value near 1 for thin or low aspect ratio clouds to almost 0.5 for the highest optical depth, largest aspect ratio clouds.

Results for the other two solar zenith angles are shown in Figures 14b and 14c. The trends at $\theta_0 = 49^\circ$ are similar to those at 0° , though the ratio does not get so small, and the sensitivity to optical depth and aspect ratio is somewhat less. At 63° the ratio is much closer to 1.0 and, in fact, higher than 1.0 for a significant portion of the field. This is due to the fact that solar energy is intercepted by cloud sides, causing the effective cloud fraction to increase with increasing solar zenith angle [e.g., *Welch and Wielicki*, 1985].

These trends suggest ways to generate a corrected retrieved optical depth based on remotely sensed cloud parameters. Two possibilities have been investigated: a one parameter least squares fit to a cloud parameter and a two parameter regression. These corrections have been applied to both the 5.7 km (scan line sample) and, by averaging, the 58 km (scene average) scales. The least squares fit is generated using half the scan line samples (10 from each scene), then tested on the other half. This provides a semblance of independent data, though the cloud fields have some coherence. The test set consists of 422 scan line samples with some cloud in them, so a 15% error reduction is significant to the 3- σ level.

Results for the one parameter correction are summarized in Figures 15a and 15b. The bias error is reduced by at least 50% in all cases. Reduction of the random error below the 3- σ level is always obtained when aspect ratio is the correction parameter, only sometimes if it is not. Interestingly, the τ distribution shape information (ν or σ) is not a particularly effective parameter in correcting the optical depth retrieval error. Physical cloud shape, as measured by aspect ratio, is slightly more effective.

To further examine this result, the analysis was repeated using only the 15 overcast scenes. The results, shown in Figures 16a and 16b, reveal that σ is an effective correction parameter for overcast clouds at higher Sun angles, but τ is most effective overall. This may be a direct consequence of the shape of the reflectance versus τ curve (see Figure 6), which causes the retrieved τ to be more sensitive to reflectance as τ increases.

Results from the two parameter regression are not

shown, but little further improvement over the one parameter method is found. The use of a linear correction with aspect ratio, summarized in Table 4, may therefore provide a simple method of improving IPA-based satellite retrievals of optical depth. Testing of these relations with additional data sets is recommended.

6. Conclusions

The SHDOM radiative transport code, a two-dimensional model using a spherical harmonic representation of the source function and a discrete ordinate quadrature to compute radiances, has been applied to the determination of satellite optical depth retrieval accuracy in the presence of horizontally inhomogeneous clouds. Forty-five Landsat scenes of oceanic boundary layer clouds provide a more realistic model of cloud variability, including various types of broken cloudiness, than has previously been available, though restricted so far to only marine boundary layer clouds. The Landsat-derived optical depth variability is turned into an extinction property field for computation by SHDOM. The computed nadir reflectance is then used to retrieve optical depth. This optical depth is compared to the original Landsat value to provide a measure of remote sensing retrieval error.

The overall error in retrieved optical depth is found to be about 6% at 0° and 49° solar zenith angles and about 2% at 63° solar zenith angle. The reduced error at 63° is caused by solar energy intercepted and reflected by the cloud sides. For broken cloud scenes and high Sun, however, this error can be as high as 45%. Examination of statistical parameters describing the cloud fields suggests that the variability of optical depth is underestimated beyond a standard deviation of 15 and especially for broken cloud fields. The width of the optical depth distribution, as measured by the gamma function parameter ν , is retrieved reasonably well, with up to 24% bias at overhead Sun, and some significant error for highly variable cloud fields ($\nu < 1$).

Corrections to the retrieved optical depth based on the observed behavior of the error with various cloud parameters have been investigated. Use of a linear correction based on aspect ratio is sufficient to obtain statistically significant improvement in the retrieved optical depth. This correction is presented for further assessment. The definition of aspect ratio developed for this study is open to improvement but is one that can be assessed from remote sensing measurements.

On the basis of the sensitivity to aspect ratio found in this study, it is recommended that some measure of cloud physical aspect ratio be included in classification of satellite cloud optical depth data when sufficiently high spatial resolution data are available.

Finally, we emphasize that all of the above conclusions are valid only for marine boundary layer clouds and were obtained assuming monochromatic, conservative scattering radiation, constant water droplet size throughout the cloud, no gas absorption, and no surface reflection. An extension of these results is under way to remove some of these constraints.

Appendix: SHDOM Algorithm

In the course of solving the radiative transfer equation, SHDOM must transform between the discrete ordinate and spherical harmonic representations. The discrete ordinates form a Gaussian grid, so that there are N_μ Gaussian quadrature cosine zenith angles, μ_j , times N_ϕ evenly spaced azimuth angles, ϕ_k (between 0 and π in two dimensions). The spherical harmonic representation has the meridional index l between 0 and L and the Fourier azimuthal mode m from 0 to M (only cosine modes are needed for two-dimensional cases because of symmetry). If $M = L$, then the spherical harmonic truncation is triangular, which has equal angular resolution in all directions. The discrete ordinate radiance I_{jk} at each grid point is transformed to spherical harmonic space according to

$$I_{lm} = \sum_{j=1}^{N_\mu} w_j \Lambda_{lm}(\mu_j) \sum_{k=1}^{N_\phi} \hat{w}_k \cos(m\phi_k) I_{jk} \quad (\text{A1})$$

where $\Lambda_{lm}(\mu)$ are the normalized associated Legendre functions, w_j are the Gauss-Legendre quadrature weights, and \hat{w}_k are the trapezoidal integration weights normalized appropriately. A fast Fourier transform is used for the azimuthal transform for larger number of angles. The computation of the source function is very fast in spherical harmonic space because the scattering integral reduces to a simple weighting by the Legendre phase function coefficients for each l [Evans, 1993]. The source function (J_{lm}) is transformed to discrete ordinates by

$$J_{jk} = \sum_{m=0}^M \cos(m\phi_k) \sum_{l=m}^L \Lambda_{lm}(\mu_j) J_{lm} \quad (\text{A2})$$

Generally, the number of discrete ordinates is chosen so $N_\mu = L + 1$ and $N_\phi = M + 2$ (in two dimensions), which assures that the spherical harmonics are

orthogonal when their product is integrated. The explicit form of the transforms is given here because it illustrates how the azimuthal and zenith angle parts partially separate, leading to a substantial decrease in the number of operations. If there are N discrete ordinates ($N = (L + 1)(M + 2)$) then using the odd-even symmetry of the associated Legendre functions, the number of floating point operations for both transforms together is about $5N^{3/2}$. The source function computation has only $1.5N$ operations. This should be contrasted with the discrete ordinate method (S-N) [Gerstl and Zardecki, 1985; Sanchez et al., 1994] in which the scattering integral takes $2N^2$ operations.

The discrete ordinate radiance field is calculated by integrating the source function weighted by transmission through the spatial grid. Each ordinate is started at the grid point locations along the appropriate boundary (top for downwelling, bottom for upwelling) and traced through the medium. The extinction and source function are interpolated from the grid points to the grid cell entrance and exit locations for the ray. The formula for the integration across a grid cell assumes a linear variation in the extinction and the source function from the entrance to exit location and uses an expansion to first order in the distance. The radiance of the ray exiting the cell is found from the integral of the source function and the transmitted entrance radiance. The radiance at the location where a ray exits a grid cell is allocated to the two points bordering the edge according to inverse square distance weighting. The accuracy of this path integration procedure depends on the assumptions of the integration formula and the radiance interpolation and requires that source function and radiance changes across a grid cell be small. This can be satisfied by making the grid cells fine enough that the optical depth across a grid cell is small compared to 1. In this study, the grid cell optical depth limit, in both x and z directions, has been set to 0.7.

The vertical boundary conditions are no reflection at the top and Lambertian reflection at the bottom boundary (although in this study the surface albedo is set to zero). There are periodic boundary conditions horizontally, so that the discrete rays wrap around until they hit the top or bottom boundary. The collimated direct solar beam is separated from the diffuse radiation, so the internal source of radiation is the singly scattered direct beam. If the delta-M method [Wiscombe, 1977] is specified, then the extinction, single-scattering albedo, and Legendre phase function coefficients are scaled before the solution it-

erations.

The solution method consists of iterations in which the radiance field is transformed to spherical harmonics, the source function is computed, the source function is transformed back to discrete ordinates, and then is integrated to get the radiance field. The source function is computed in spherical harmonic space by adding the fixed single-scattered source of diffuse radiation to the scattering integral. This solution method is effectively an order of scattering approach (or Λ iteration in the astrophysical literature), and convergence is slower for optically thicker or less absorbing media. A simple acceleration method is used to reduce the number of iterations required, by extrapolating the radiance field from the previous field when the convergence is suitably geometric. The iterations are stopped when the solution criterion, which is the normalized root-mean-square (RMS) difference between successive radiance fields, is below some value. In this work, the criterion is $1.e-4$.

The radiance at specified angles and locations is computed after convergence of the solution by integrating the source function. The spherical harmonic representation of the radiance field is transformed to the source function for the viewing angle. When using the delta-M method as done here, the TMS method of Nakajima and Tanaka [1988] is used to compute the radiance. This simply replaces the scaled, truncated Legendre phase function expansion for the singly scattered solar radiation by the full, unscaled phase function expansion. The multiply scattered contribution still comes from the truncated phase function. The TMS method is quite accurate for the backscattering directions encountered in satellite remote sensing. The source function is integrated backward from the top of the atmosphere, assuming bilinear interpolation of the extinction and source function within each grid cell, to obtain the upwelling radiance. A newer version of SHDOM (K. Evans, The spherical harmonics discrete ordinate method for three-dimensional atmospheric radiative transfer, submitted to *Journal of the Atmospheric Sciences*, 1996) uses an adaptive grid to place grid cells where they are most needed and has a number of other major changes.

Acknowledgments. Paul Stackhouse, of Colorado State University, provided valuable assistance in learning to run the SHDOM model. Lindsay Parker, of Science Applications International Corp, (SAIC), processed the Landsat reflectances into the cloud optical depths and thresholds used in this study. Robert Arduini, also of SAIC, provided the Legendre coefficients of the Mie phase

function. Howard Barker of Atmospheric Environment Service provided the fractal cascade model used in section 2.3.3 as well as valuable discussions. An anonymous reviewer provided a number of helpful comments.

References

- Barker, H. W., B. A. Wielicki, and L. Parker, A parameterization for computing grid-averaged solar fluxes for inhomogeneous marine boundary layer clouds, II, Validation using satellite data, *J. Atmos. Sci.*, 53, 2304, 1996.
- Baum, B. A., P. Minnis, J. A. Coakley Jr., B. A. Wielicki, P. Menzel, J. Titlow, V. Tovinkere, P. Heck, and S. Mayor, Imager cloud height determination (subsystem 4.2), in *Clouds and the Earth's Radiant Energy System (CERES) Algorithm Theoretical Basis Document*, Vol. III, *Cloud Analyses and Determination of Improved Top of Atmosphere Fluxes* (subsystem 4), NASA RP 1376, pp. 83-134, 1995.
- Cahalan, R. F., and J. B. Snider, Marine stratocumulus structure, *Remote Sens. Environ.*, 28, 95, 1989.
- Cahalan, R. F., W. Ridgway, W. J. Wiscombe, T. L. Bell, and J. B. Snider, The albedo of fractal stratocumulus clouds, *J. Atmos. Sci.*, 51, 2434, 1994a.
- Cahalan, R. F., W. Ridgway, W. J. Wiscombe, S. Gollmer, and Harshvardhan, Independent pixel and Monte Carlo estimates of stratocumulus albedo, *J. Atmos. Sci.*, 3776, 1994b.
- Davies, R., The effect of finite geometry on the three-dimensional transfer of solar irradiance in clouds, *J. Atmos. Sci.*, 35, 1712, 1978.
- Davis, A., A. Marshak, W. Wiscombe, and R. Cahalan, Scale invariance of liquid water distributions in marine stratocumulus, I, Spectral properties and stationarity issues, *J. Atmos. Sci.*, 53, 1538, 1996.
- Duda, D. P., and G. L. Stephens, Macrophysical and microphysical influences on radiative transfer in two dimensional marine stratus, *Atmos. Sci. Pap.* 565, Colo. State Univ., 1994.
- Evans, K. F., Two-dimensional radiative transfer in cloudy atmospheres: The spherical harmonics spatial grid method, *J. Atmos. Sci.*, 50, 3111, 1993.
- Gabriel, P. M., S.-C. Tsay, and G. L. Stephens, A Fourier-Riccati approach to radiative transfer, I, Foundations, *J. Atmos. Sci.*, 50, 3125, 1993.
- Gerstl, S. A. W., and A. Zardecki, Discrete-ordinates finite-element method for atmospheric radiative transfer and remote sensing, *Appl. Opt.*, 24, 81, 1985.
- Harshvardhan, B. A. Wielicki, and K. M. Ginger, The interpretation of remotely sensed cloud properties from a model parameterization perspective, *J. Clim.*, 7, 1987, 1994.
- Kobayashi, T., Effects due to cloud geometry on biases in the albedo derived from radiance measurements, *J. Clim.*, 6, 120, 1993.
- Killen, R. M., and R. G. Ellingson, The effect of shape and spatial distribution of cumulus clouds on longwave irradiance, *J. Atmos. Sci.*, 51, 2123, 1994.
- Leith, C. E., The standard error of time-average estimates of climatic means, *J. Appl. Meteorol.*, 12, 1066, 1973.
- Marshak, A., A. Davis, W. Wiscombe, and R. Caha-

- lan, Radiative smoothing in fractal clouds, *J. Geophys. Res.*, **100**, 26,247, 1995a.
- Marshak, A., A. Davis, W. Wiscombe, and G. Titov, The verisimilitude of the independent pixel approximation used in cloud remote sensing, *Remote Sens. Environ.*, **52**, 71, 1995b.
- McKee, T. B., and S. K. Cox, Scattering of visible radiation by finite clouds, *J. Atmos. Sci.*, **31**, 1885, 1974.
- Minnis, P., P. W. Heck, D. F. Young, C. W. Fairall, and B. J. Snider, Stratocumulus cloud properties derived from simultaneous satellite and island-based instrumentation during FIRE, *J. Appl. Meteorol.*, **31**, 317, 1992.
- Nakajima, T., and M. Tanaka, Algorithms for radiative intensity calculations in moderately thick atmospheres using a truncation approximation, *J. Quant. Spectrosc. Radiat. Transfer*, **40**, 51, 1988.
- Nakajima, T., M. D. King, J. D. Spinhirne, and L. F. Radke, Determination of the optical thickness and effective particle radius of clouds from reflected solar radiation measurements, II, Marine stratocumulus observations, *J. Atmos. Sci.*, **48**, 728, 1991.
- Pincus, R., M. Szczodrak, J. Gu, and P. Austin, Uncertainty in cloud optical depth estimates made from satellite radiance measurements, *J. Clim.*, **8**, 1453, 1995.
- Rossow, W. B., L. C. Garder, P. J. Lu, and A. Walker, International Satellite Cloud Climatology Project (ISCCP) documentation of cloud data, *WMO/TD-266*, Geneva, 1991.
- Sanchez, A., T. F. Smith, and W. F. Krajewski, A three-dimensional atmospheric radiative transfer model based on the discrete ordinates method, *Atmos. Res.*, **33**, 283, 1994.
- Stackhouse, P. W., Jr., On the effects of cloud inhomogeneity upon ice cloud radiative properties, Ph.D. dissertation, Colo. State Univ., Fort Collins, 1995.
- Takara, E. E., and R. G. Ellingson, Scattering effects on longwave fluxes in broken cloud fields, *J. Atmos. Sci.*, **53**, 1464, 1996.
- Tsay, S.-C., K. Stamnes, and K. Jayaweera, Radiative transfer in stratified atmospheres: Development and verification of a unified model, *J. Quant. Spectrosc. Radiat. Transfer*, **43**, 133, 1990.
- Welch, R. M., and B. A. Wielicki, Stratocumulus cloud field reflected fluxes: The effect of cloud shape, *J. Atmos. Sci.*, **41**, 3085, 1984.
- Welch, R. M., and B. A. Wielicki, A radiative parameterization of stratocumulus cloud fields, *J. Atmos. Sci.*, **42**, 2888, 1985.
- Wielicki, B. A. and L. Parker, On the determination of cloud cover from satellite sensors: The effect of sensor spatial resolution, *J. Geophys. Res.*, **97**, 12,799, 1992.
- Wielicki, B. A. and L. Parker, Frequency distributions of cloud liquid water path in oceanic boundary layer cloud as a function of regional cloud fraction, paper presented at the 8th Conference on Atmospheric Radiation, Am. Meteor. Soc., Nashville, Tenn., Jan 23-28, 1994.
- Wiscombe, W. J., The delta-M method: Rapid yet accurate radiative flux calculations for strongly asymmetric phase functions, *J. Atmos. Sci.*, **34**, 1408, 1977.
- L. H. Chambers and B. A. Wielicki, Atmospheric Sciences Division, MS 420, NASA Langley Research Center, Hampton, VA 23681-0001. (e-mail: l.h.chambers@larc.nasa.gov, b.a.wielicki@larc.nasa.gov)
- K. F. Evans, Program in Atmospheric and Oceanic Sciences, University of Colorado, Boulder, CO 80309-0311. (e-mail: evans@nit.colorado.edu)
- March 22, 1996; revised September 26, 1996; accepted September 26, 1996.

<u>Input</u>		<u>Process</u>	<u>Output</u>
1)	$R_{\text{Landsat}}(x)$	→ IPA	→ $\tau_{\text{ref}}(x)$
2)	$\tau_{\text{ref}}(x)$	→ $\Delta z(\tau)$	→ $\beta(x, z)$
3)	$\beta(x, z)$	→ 2D SHDOM	→ $R_{2D}(x) \neq R_{\text{Landsat}}(x)$
4)	$R_{2D}(x)$	→ IPA	→ $\tau_{\text{IPA}}(x)$
5)	$\tau_{\text{IPA}}(x) - \tau_{\text{ref}}(x)$	→ PLOT	→ error statistics

Figure 1. Processes applied in this study with input to and output from each step.

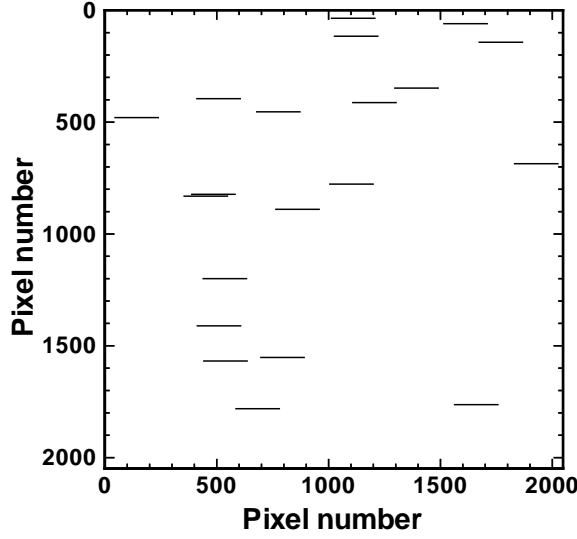


Figure 2. Twenty randomly selected 5.7 km (200 pixel) scan line samples in a 58 by 58 km Landsat scene provide adequate subsampling of the field.

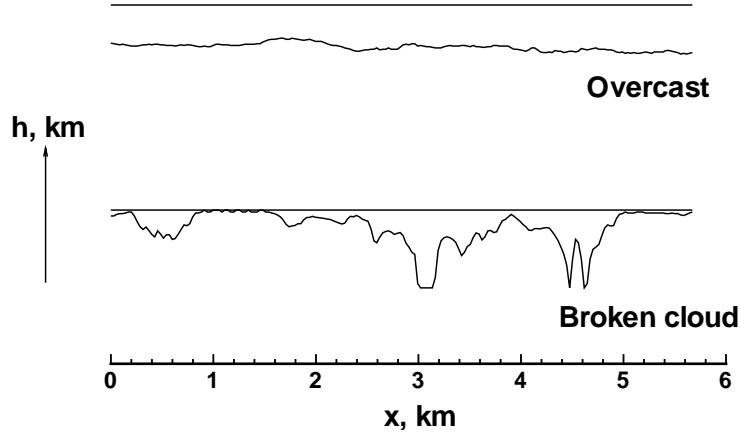


Figure 3. Typical cloud profiles along a scan line sample show the extremes, from complete overcast to broken cloud, covered in this data set.

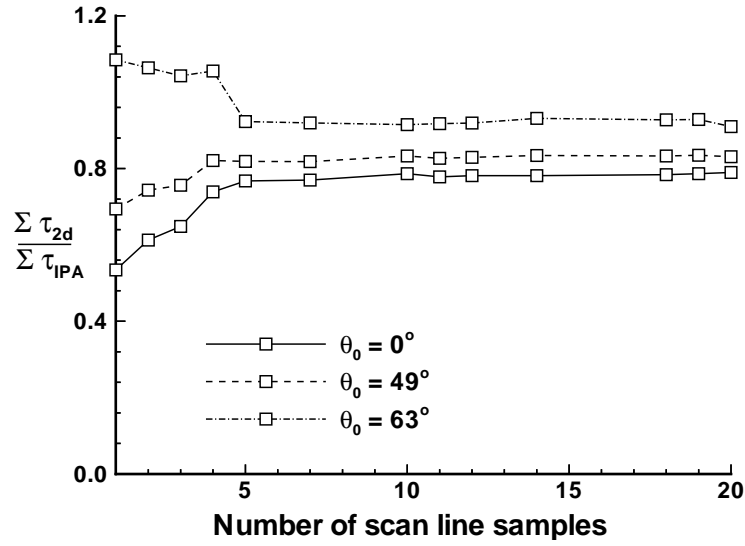


Figure 4. Typical sample convergence for a Landsat scene. All 45 cases converge with less than 15 samples.

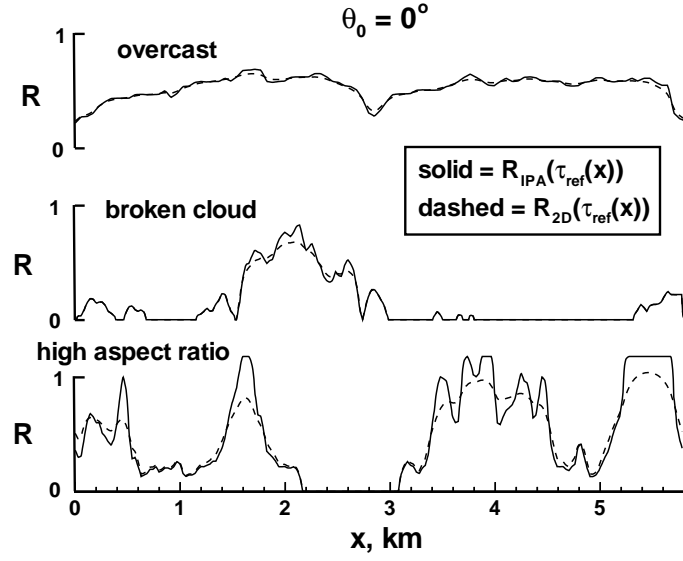


Figure 5. Example scan lines showing the variation of two-dimensional and independent pixel approximation (IPA)-calculated nadir reflectance given the same Landsat-derived $\tau_{\text{ref}}(x)$ as input.

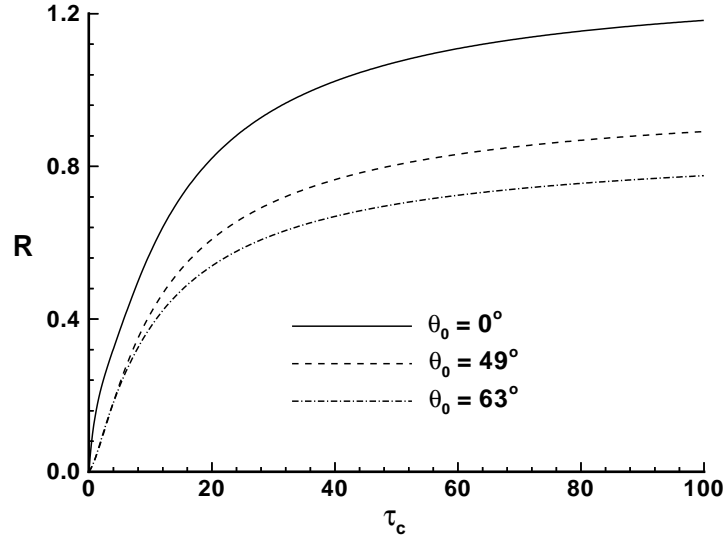


Figure 6. IPA calculations of nadir reflectance as a function of τ_c and θ_0 . The IPA cloud retrieval uses this relationship to convert each Landsat-measured reflectance to an equivalent τ_{IPA} .

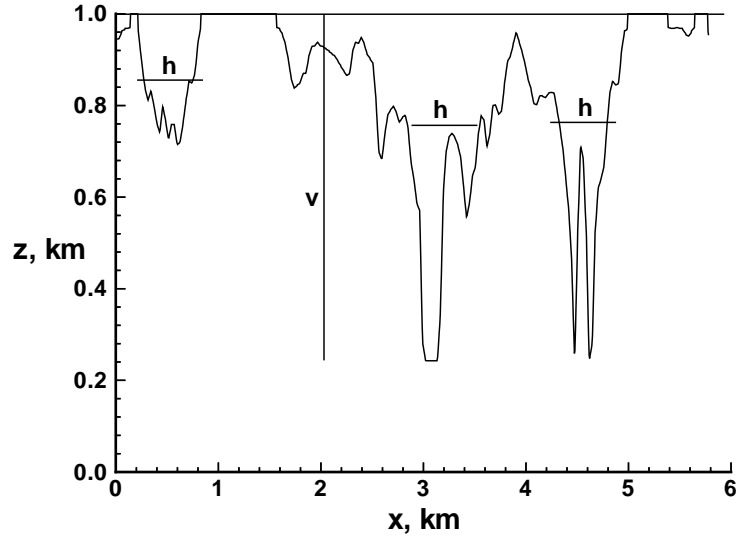


Figure 7. Example of aspect ratio (v/h) estimation using equation (6) for Landsat scan line sample.

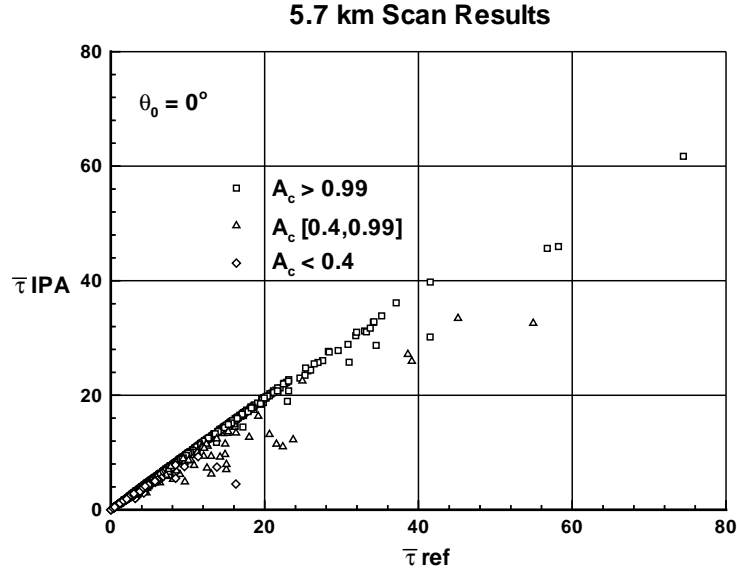


Figure 8a. Scatterplot of $\bar{\tau}_{IPA}$ versus $\bar{\tau}_{ref}$ at 5.7 km scan line sample level, $\theta_0 = 0^\circ$.

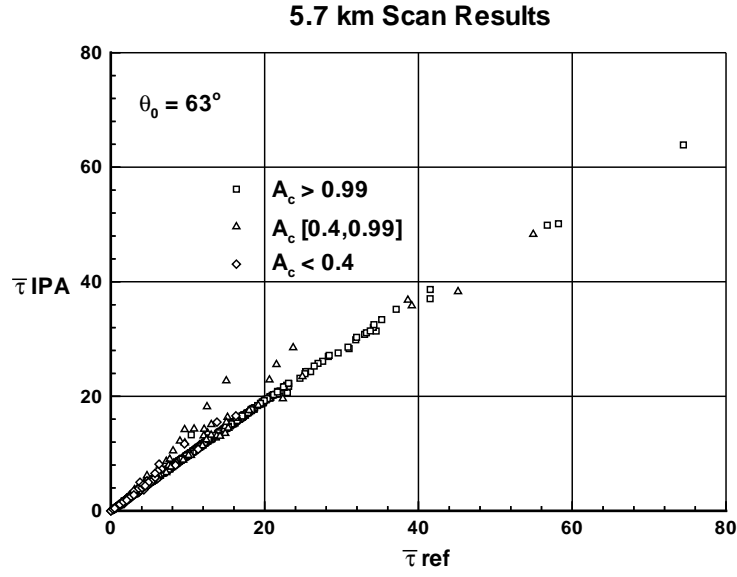


Figure 8b. As in (a) but for $\theta_0 = 63^\circ$.

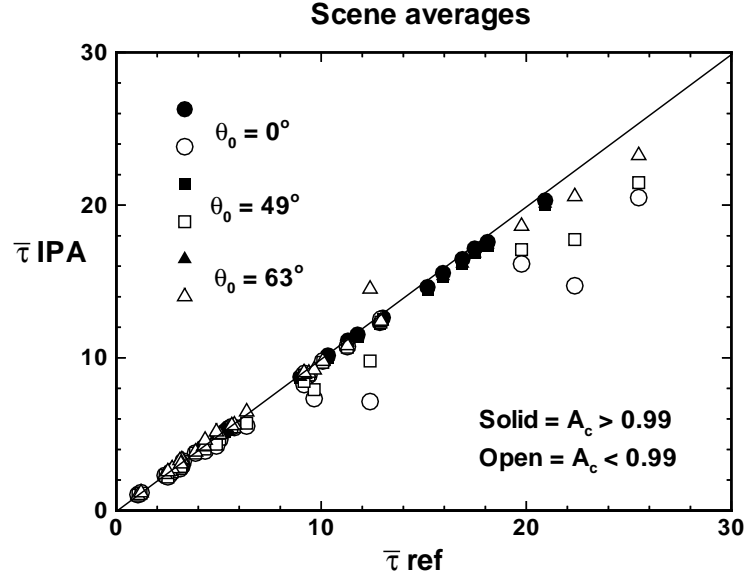


Figure 9. Scatterplot of $\bar{\tau}_{\text{IPA}}$ versus $\bar{\tau}_{\text{ref}}$ for each 58 by 58 km scene.

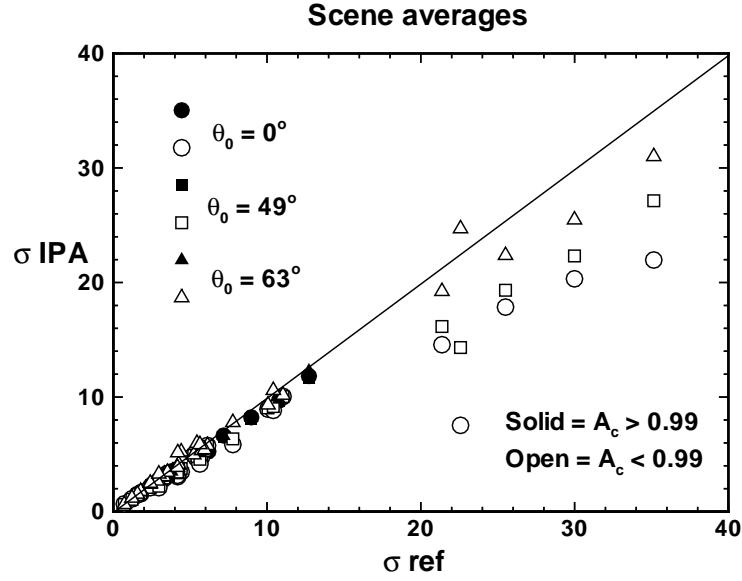


Figure 10. Scatterplot of the standard deviation of τ_{IPA} versus $\sigma(\tau_{\text{ref}})$ for each 58 by 58 km scene.

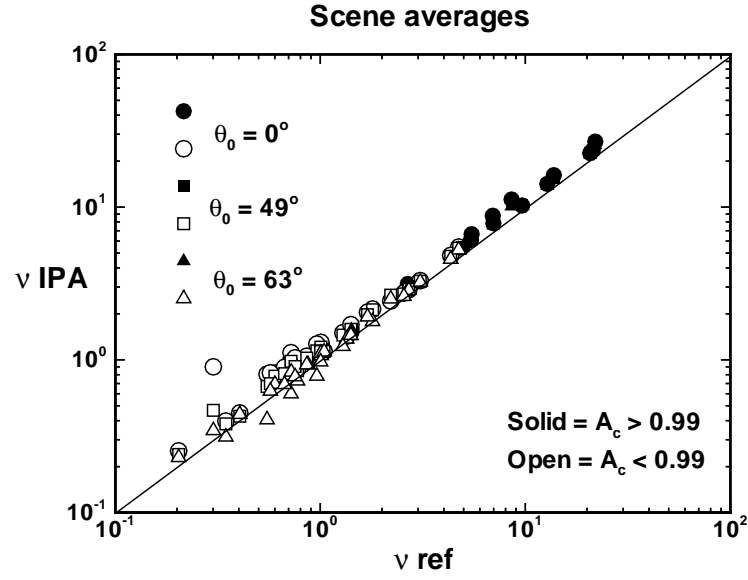


Figure 11. Scatterplot of gamma function parameter ν_{IPA} versus ν_{ref} for each 58 by 58 km scene.

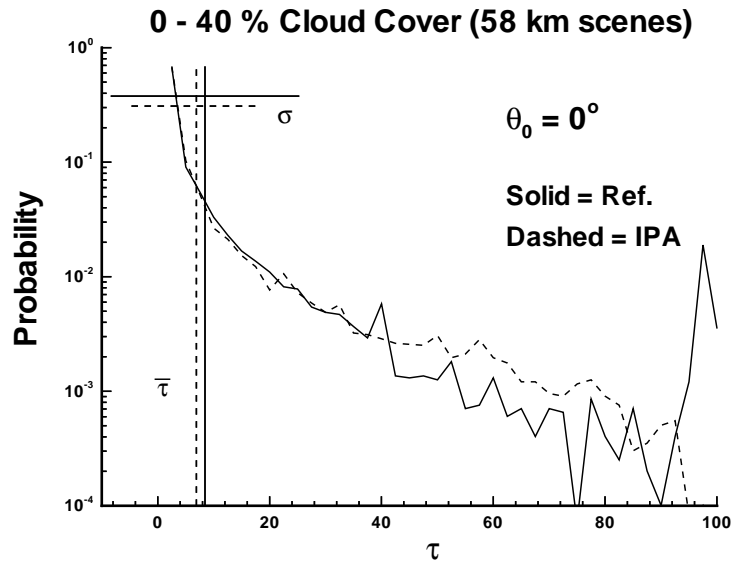


Figure 12a. Reference and IPA probability distribution of optical depths composited for scenes with cloud fraction of 0 to 40% with mean and standard deviation.

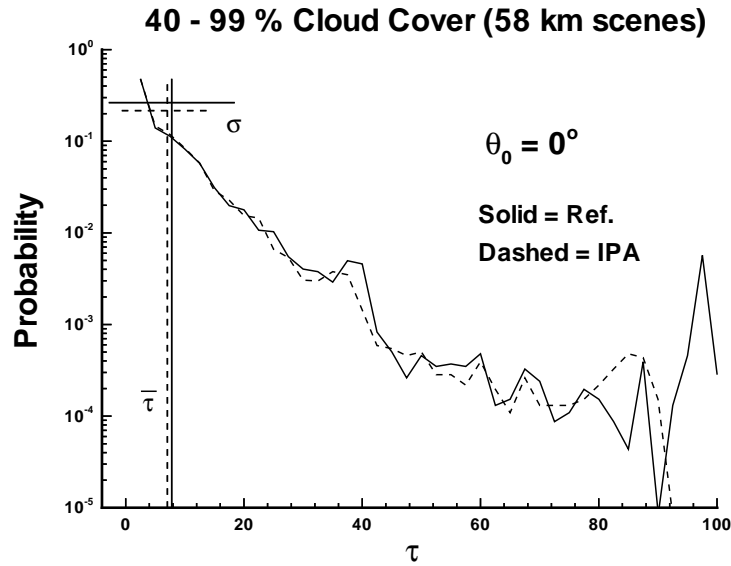


Figure 12b. As in (a) but for scenes with cloud fraction of 40 to 99%.

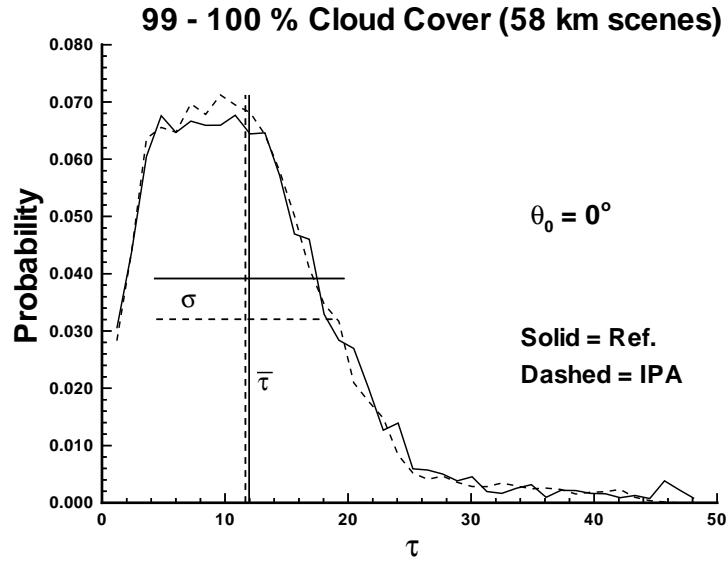


Figure 12c. As in (a) but for scenes with cloud fraction of 99 to 100%.

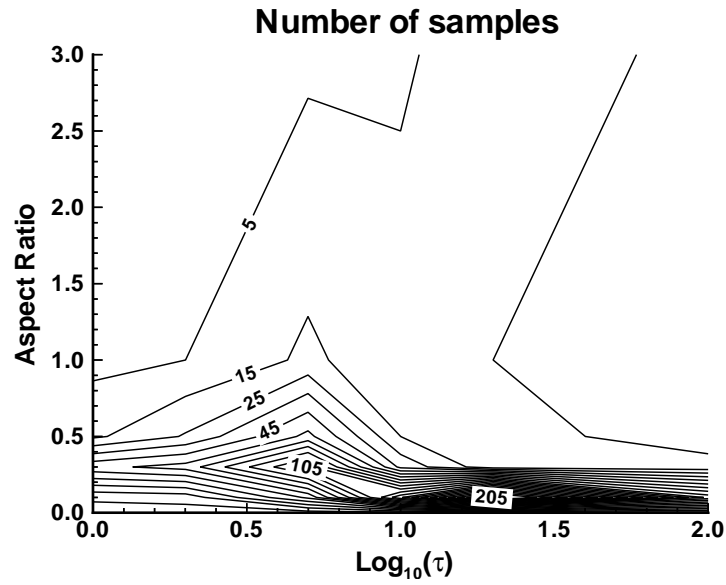


Figure 13. Number of scan line samples in aspect ratio - $\log_{10}(\tau)$ space.

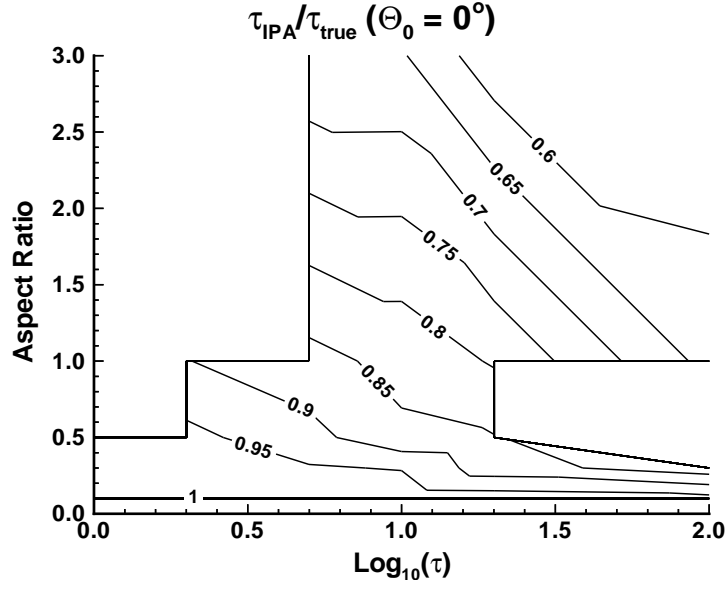


Figure 14a. Average τ_{IPA}/τ_{ref} in aspect ratio - $\log_{10}(\tau)$ space, $\theta_0 = 0^\circ$.

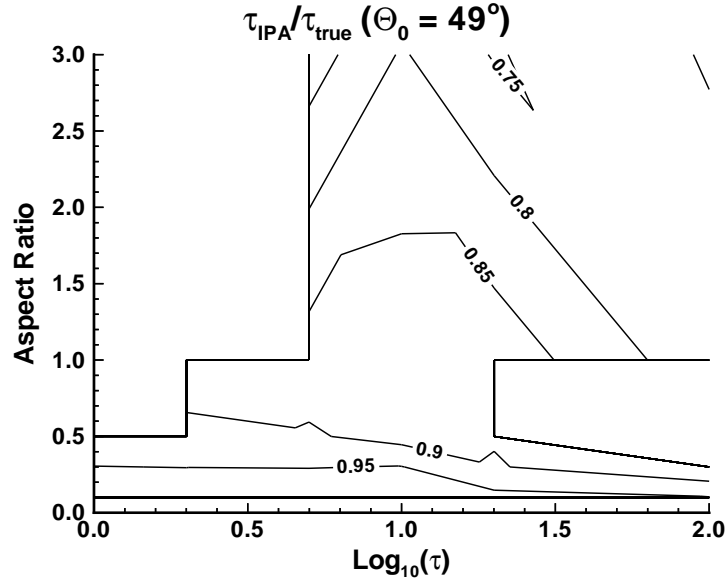


Figure 14b. As in (a) but for $\theta_0 = 49^\circ$.

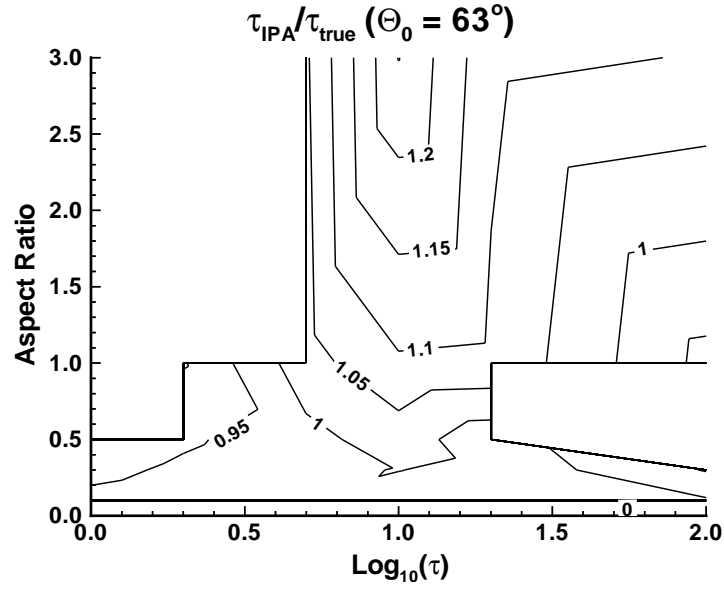


Figure 14c. As in (a) but for $\theta_0 = 63^\circ$.

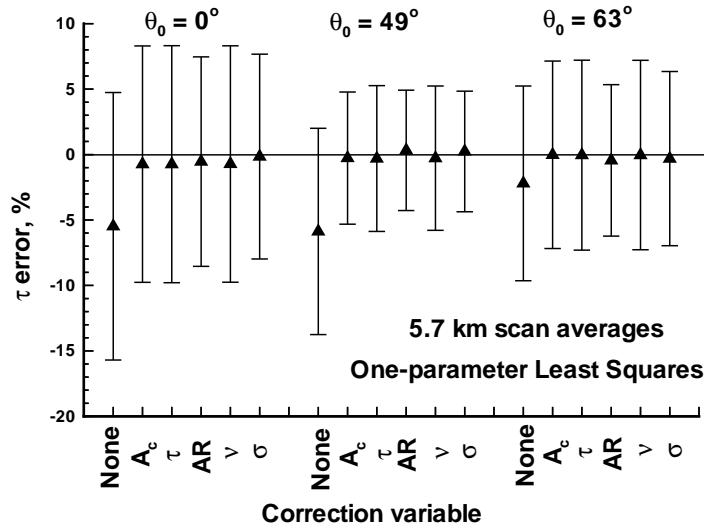


Figure 15a. Summary of mean and RMS optical depth errors using least squares fits with various cloud parameters compared with the uncorrected error. All scenes at scan line sample (5.7 km) scale.

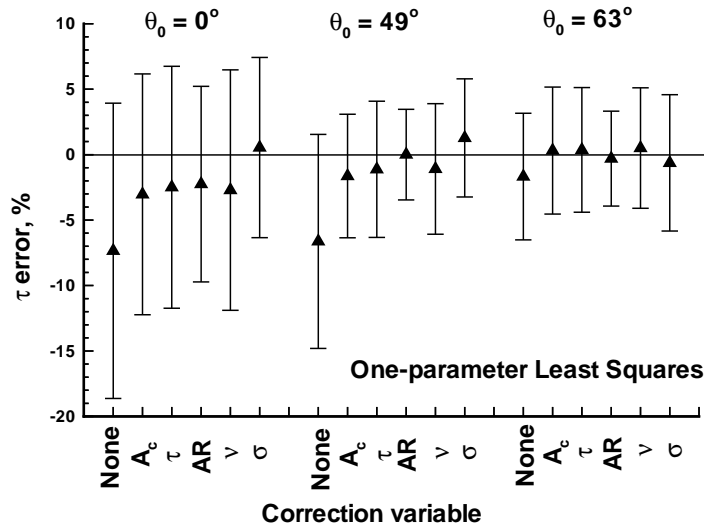


Figure 15b. As in (a) but at scene average (58 km) scale.

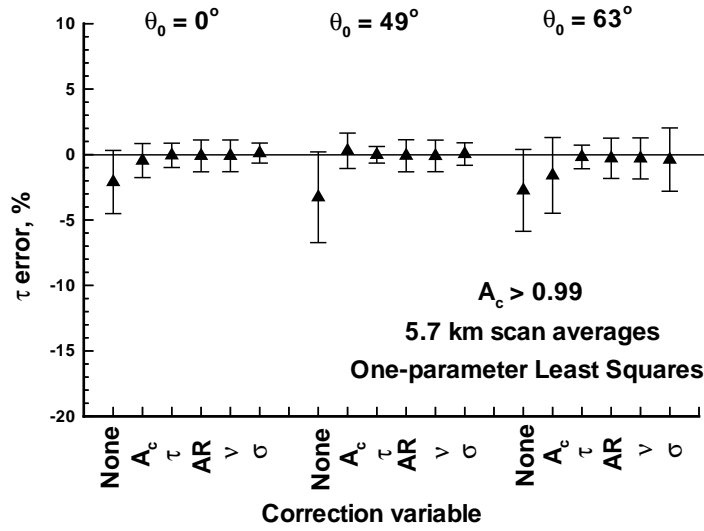


Figure 16a. Summary of mean and RMS optical depth errors using least squares fits with various cloud parameters compared with the uncorrected error. Overcast scenes only at scan line sample (5.7 km) scale.

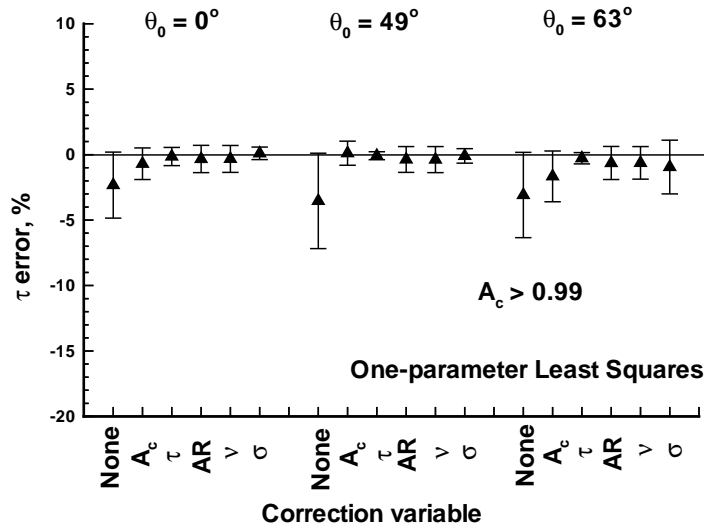


Figure 16b. As in (a) but at scene average (58 km) scale.

Plate 1. Typical variety of cloud scenes in Landsat data set used in this paper. First column represents trade cumulus, second column broken stratocumulus, and third column solid stratocumulus.

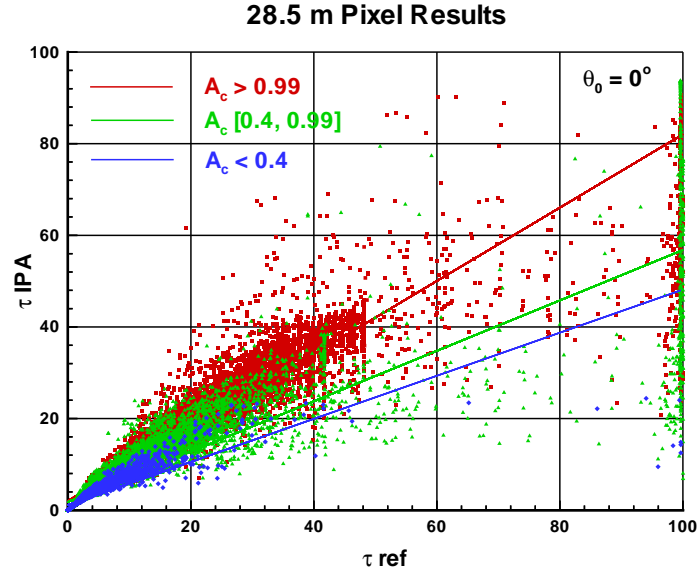


Plate 2a. Scatterplot of τ_{IPA} versus τ_{ref} at 28.5 m pixel level, $\theta_0 = 0^\circ$.

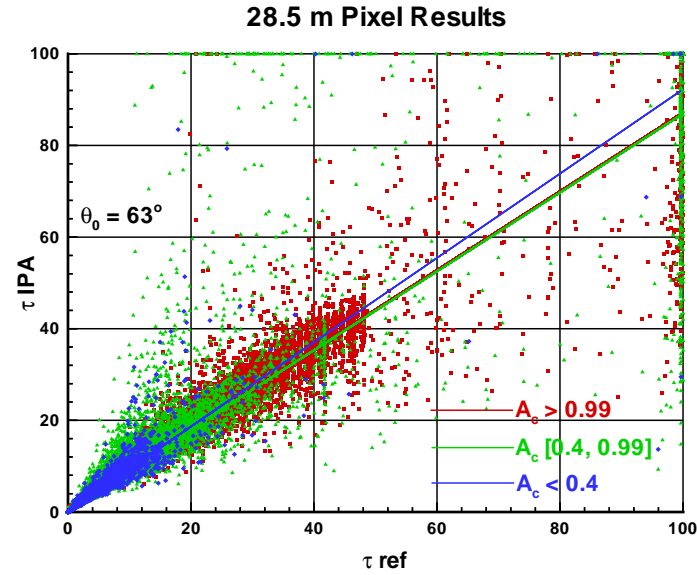


Plate 2b. As in (a) but for $\theta_0 = 63^\circ$.

Table 1. Identification of the Location and Time of Additional Landsat Scenes Analyzed in This Study.

Scene	Date	Lat/Long, deg	Time, UTC	θ_0 , deg	Cloud Fraction	$\bar{\tau}$
46	1 June 92	36.0°N/23.7°W	1117	32	1.000	13.8
47	12 June 92	33.2°N/19.9°W	1059	32	0.920	5.7
48	12 June 92	36.1°N/19.1°W	1100	32	1.000	17.0
49	14 June 92	33.2°N/16.8°W	1047	32	0.363	5.3
50	17 June 92	34.6°N/24.1°W	1118	32	1.000	18.6
51	21 June 92	33.2°N/18.3°W	1053	32	0.998	14.6
52	21 June 92	34.6°N/17.8°W	1054	32	1.000	20.5

Also tabulated are the solar zenith angle θ_0 , cloud fraction, and cloudy pixel mean optical depth $\bar{\tau}$.

Table 2. Pixel Level Statistics for Independent Pixel Approximation (IPA) Errors

	$0 < A_c < 0.4$	$0.4 < A_c < 0.99$	$0.99 < A_c < 1.$
n	16	14	15
$\langle \bar{\tau}_c \rangle$	7.88	8.38	12.6
$\sigma(\pi_{\text{IPA}} - \tau_{\text{ref}})[\theta_0 = 0^\circ]$	7.48	4.98	1.19
$\sigma(\pi_{\text{IPA}} - \tau_{\text{ref}})[\theta_0 = 49^\circ]$	6.09	3.93	1.11
$\sigma(\pi_{\text{IPA}} - \tau_{\text{ref}})[\theta_0 = 63^\circ]$	6.49	4.49	1.35

Table 3. Mesoscale Level Statistics for IPA Errors

	$0 < A_c < 0.4$	$0.4 < A_c < 0.99$	$0.99 < A_c < 1.$
n	16	14	15
$\langle \bar{\tau}_c \rangle$	7.30 ± 7.20	8.27 ± 4.50	12.6 ± 4.78
$\langle \nu \rangle$	0.72 ± 0.36	1.92 ± 1.29	9.45 ± 6.68
$\langle A_c \rangle$	0.29 ± 0.09	0.82 ± 0.15	0.998 ± 0.003
$\theta_0 = 0^\circ$			
$\overline{(\tau_{\text{IPA}} - \tau_{\text{ref}})}$	-1.24	-0.84	-0.32
$\sigma(\tau_{\text{IPA}} - \tau_{\text{ref}})$	2.11	1.56	0.19
$\overline{(\nu_{\text{IPA}} - \nu_{\text{ref}})}$	0.21	0.30	1.47
$\sigma(\nu_{\text{IPA}} - \nu_{\text{ref}})$	0.10	0.20	1.27
$\theta_0 = 49^\circ$			
$\overline{(\tau_{\text{IPA}} - \tau_{\text{ref}})}$	-0.91	-0.61	-0.48
$\sigma(\tau_{\text{IPA}} - \tau_{\text{ref}})$	1.39	0.87	0.26
$\overline{(\nu_{\text{IPA}} - \nu_{\text{ref}})}$	0.15	0.23	1.34
$\sigma(\nu_{\text{IPA}} - \nu_{\text{ref}})$	0.10	0.16	1.17
$\theta_0 = 63^\circ$			
$\overline{(\tau_{\text{IPA}} - \tau_{\text{ref}})}$	-0.24	-0.09	-0.42
$\sigma(\tau_{\text{IPA}} - \tau_{\text{ref}})$	0.72	0.71	0.24
$\overline{(\nu_{\text{IPA}} - \nu_{\text{ref}})}$	0.004	0.13	0.99
$\sigma(\nu_{\text{IPA}} - \nu_{\text{ref}})$	0.11	0.14	0.88

Table 4. Linear Correction for Retrieved Optical Depth Based on Aspect Ratio^a

θ_0	Correction for τ
0.	$\tau_{\text{meas}} / (0.995 - 0.283 \overline{(v/h)})$
49.	$\tau_{\text{meas}} / (0.981 - 0.241 \overline{(v/h)})$
63.	$\tau_{\text{meas}} / (0.951 - 0.154 \overline{(v/h)})$

^a $\overline{(v/h)}$, equation (6)